

A GPU-Enabled, High-Resolution Cosmological Microlensing Parameter Survey*

N. F. Bate^{1,2} and C. J. Fluke¹

¹*Centre for Astrophysics & Supercomputing, Swinburne University of Technology, PO Box 218, Hawthorn, Victoria, 3122, Australia*

²*Sydney Institute for Astronomy, School of Physics, A28, University of Sydney, NSW, 2006, Australia*

cfluke@swin.edu.au

ABSTRACT

In the era of synoptic surveys, the number of known gravitationally lensed quasars is set to increase by over an order of magnitude. These new discoveries will enable a move from single-quasar studies to investigations of statistical samples, presenting new opportunities to test theoretical models for the structure of quasar accretion discs and broad emission line regions (BELRs). As one crucial step in preparing for this influx of new lensed systems, a large-scale exploration of microlensing convergence-shear parameter space is warranted, requiring the computation of $O(10^5)$ high resolution magnification maps. Based on properties of known lensed quasars, and expectations from accretion disc/BELR modelling, we identify regions of convergence-shear parameter space, map sizes, smooth matter fractions, and pixel resolutions that should be covered. We describe how the computationally time-consuming task of producing ~ 290000 magnification maps with sufficient resolution (10000^2 pixel/map) to probe scales from the inner edge of the accretion disc to the BELR can be achieved in ~ 400 days on a 100 teraflop/s high performance computing facility, where the processing performance is achieved with graphics processing units. We illustrate a use-case for the parameter survey by investigating the effects of varying the lens macro-model on accretion disc constraints in the lensed quasar Q2237+0305. We find that although all constraints are consistent within their current error bars, models with more densely packed microlenses tend to predict shallower accretion disc radial temperature profiles. With a large parameter survey such as the one described here, such systematics on microlensing measurements could be fully explored.

*Research undertaken as part of the Commonwealth Cosmology Initiative (CCI: www.thecci.org), an international collaboration supported by the Australian Research Council.

Subject headings: gravitational lensing: micro – quasars: individual (Q2237+0305)

1. Introduction

Cosmological gravitational microlensing refers to the regime of gravitational lensing where individual stars within a lensing galaxy act to magnify a background source, usually a quasar. The most obvious effect of microlensing is to produce an uncorrelated brightness change with time in a single image of a multiply-imaged source; an intrinsic variation in source flux would appear in all images separated by the individual image time delays. Cosmological microlensing was first observed in the lensed quasar Q2237+0305 by Irwin et al. (1989), and it is likely to be taking place on some level in all quasars multiply imaged by a foreground galaxy. For recent summaries, see Wambsganss (2006) and Schmidt & Wambsganss (2010).

While gravitational microlensing is achromatic, the magnitude of microlensing-induced fluctuations depends strongly on the size of the emission region. Small sources (relative to the Einstein radius of the microlenses) are affected more strongly than larger sources. Detections of microlensing signals in a single waveband can therefore be used to constrain the size of the quasar emission region. For example, optical observations of Q2237+0305 suggest a V-band accretion disc radius of $R_V = 6.2_{-2.7}^{+3.8} \times 10^{15}$ cm (Poindexter & Kochanek 2010b).

Multi-wavelength observations present an opportunity to constrain the wavelength-dependent structure of quasar emission regions. First constraints on the temperature profile of quasar accretion discs have already been published (Anguita et al. 2008; Bate et al. 2008; Eigenbrod et al. 2008; Poindexter et al. 2008; Floyd et al. 2009; Blackburne et al. 2011; Mediavilla et al. 2011; Mosquera et al. 2011a).

Interpretation of broad emission line region (BELR) signals are more complex, however some early attempts have been made. Lewis et al. (1998) and Wayth et al. (2005) measured the relative sizes of the CIII]/MgII BELR and continuum emission region in Q2237+0305 using microlensing observations. Abajas et al. (2007) proposed a biconical BELR as a possible explanation for a recurrent blue-wing enhancement in the emission lines of SDSS J1004+4112 (Richards et al. 2004; Gómez-Álvarez et al. 2006). O’Dowd et al. (2010) compared a differential microlensing signal observed across the CIII] emission line in Q2237+0305 with various BELR geometries, and Sluse et al. (2011) studied the broad emission lines in 39 epochs of Q2237+0305 data obtained with the VLT.

While ~ 100 multiply imaged quasars have now been discovered,¹ only ~ 20 of these have measured light travel time delays between lensed images – see Oguri (2007) for a recent compilation. New, high-cadence, all-sky surveys such as those planned for the SkyMapper Telescope (Keller et al. 2007) and the Large Synoptic Survey Telescope (LSST; Ivezić et al. 2008) are likely to discover a large number of gravitationally lensed quasars. For example, Oguri & Marshall (2010) predict that LSST will find approximately 8000 new lensed quasars across its 10-year 20000-deg² survey, 3000 of which will have good measurements of the time delays between images.

The anticipated increase in the number of known lensed quasars will take measurements of quasar structure beyond the realm of single-object studies and into that of statistically meaningful samples. For example, we can test whether a single accretion mechanism is consistent with all observations, examine scaling relations between black hole mass and accretion disc radii [see Morgan et al. (2010) for such an analysis with a sample of 11 lensed quasars], and investigate secondary parameters such as Eddington ratio (e.g Mosquera et al. 2011b).

Analysis and interpretation of this wealth of new information regarding quasar emission regions will require extensive simulations. The basic tool for microlensing is the magnification map: a pixellated approximation to a region of the (background) source plane, with a magnification value defined at each physical source location. By convolving magnification maps with wavelength-dependent geometric model profiles, both simulated lightcurves and statistical magnification distributions can be extracted, ready for comparison with observational data.

The characteristic caustic structure of a magnification map depends on the convergence and shear (described in Section 2). These parameters are local properties of the global macro-lens model at the position of each lensed image. Since each lensing environment is unique, potentially ~ 6800 new combinations of convergence and shear will need to be simulated [Oguri & Marshall (2010) predict ~ 14 per cent of ~ 3000 LSST-discovered systems will be quadruply imaged, with the remaining systems dominated by double images, resulting in a mean image number of 2.28]. Moreover, macro-lens models are not uniquely determined. For example, Witt et al. (1995) modeled lensing systems with three different lens potentials and Wyithe et al. (2002) contains a compilation of lens models for Q2237+0305 by eight different authors: each of which predicts different convergence and shear values for the lensed images. The potential need for multiple models, and hence magnification maps, for each newly discovered system further increases the expected coverage of convergence-shear

¹See the CASTLES Survey webpage: <http://www.cfa.harvard.edu/glensdata/>

parameter space.

Although the computational time needed for analysis of magnification maps can be considerable (e.g. Poindexter & Kochanek 2010a), generating sufficient high-resolution, statistically useful magnification maps is itself a computationally-demanding task. Over the last two decades, the most widely-used approaches to generating magnification maps are based on backwards ray-shooting (described in more detail in Section 2). Here, light rays are propagated from the observer, through the lens plane, requiring the calculation of deflections by N_* individual lenses, and mapped onto the pixellated source plane. This computation is repeated for a sufficiently large number of light rays, typically $O(10^6)$ or higher, in order to achieve statistically significant coverage per pixel in the source plane.

In the hierarchical tree method (Wambsganss 1990; Wambsganss 1999), individual lenses are approximated by higher-mass pseudo-lenses, depending on their distance from a given light ray, thus avoiding the requirement for N_* deflection calculations per light ray. Kochanek (2004) describes a computationally-efficient approach to reducing the N_* effect, where the lens and source planes are treated as spatially periodic, allowing the use of Fourier methods (similar to the P³M methods used for many-particle gravitational force computations). Mediavilla et al. (2006) and Mediavilla et al. (2011) adaptively tessellate the lens plane, with the lens equation used to map the lattice of polygons from the image to source plane, where the polygons are efficiently mapped onto source pixels. This approach reduces the total number of light rays required to reach a given statistical accuracy by over three orders of magnitude.

The emergence of the graphics processing unit (GPU) as a means of accessing low cost, high performance, massively parallel computing, presents an alternative opportunity for speeding-up deflection angle calculations with an algorithmically-simple solution. Astronomers have been amongst the early adopters of GPUs for scientific computation, reporting typical speed-ups between $\times 30$ to $\times 100$ over what they can achieve on single (or few) core CPUs. While further work is required to fully understand which types of computations are best suited for GPUs [see Barsdell et al. (2010) and Fluke et al. (2011) for a discussion of these issues specifically aimed at astronomers], algorithms that exhibit the properties of high arithmetic intensity and a high-level of data parallelism are the most promising targets.

Thompson et al. (2010) demonstrated that by taking advantage of the highly parallel GPU-architecture, a “brute force” implementation of ray-shooting is now a practical alternative. Moreover, Bate et al. (2010) have shown that on current generation multi-GPU systems (e.g. the 4-GPU NVIDIA Tesla S1070 unit with a processing peak of ~ 2.5 teraflop/s for

single precision computation²), the direct code on GPU executes in runtimes comparable too, and often faster than, the single-core tree code.

Our target system is the Australian GPU Supercomputer for Theoretical Astrophysics Research (gSTAR³), a hybrid CPU+GPU cluster containing $102 \times$ NVIDIA C2070 GPUs and $21 \times$ M2090 GPUs, connected via QDR Infiniband, with a (theoretical, single-precision) peak of ~ 130 teraflop/s. Throughout this work, we estimate run-times for two different GPU cluster configurations: we assume a slightly more conservative 100 teraflop/s mode of operation for the phase one gSTAR system, gSTAR₁₀₀, and a somewhat optimistic future upgrade with a peak of 600 teraflop/s, gSTAR₆₀₀, based on the original system design goals. In both cases, we expect to achieve at least 50 per cent of the theoretical peak, based on the benchmarking in Thompson et al. (2010).

Our goal in this paper is to demonstrate that a high resolution, large-scale, microlensing parameter survey is feasible on a GPU-enabled computing cluster. This requires generating statistically useful samples of high-resolution magnification maps over the entire range of convergence-shear parameter space – a theoretical equivalent of an “all-sky” survey. By providing ~ 290000 pre-computed magnification maps as a Web-accessible resource, rapid first look computations would be possible as new microlensed quasars are discovered. High-resolution coverage of parameter space enables investigation of degeneracies between macro-model parameters and inferred plausible models for quasar emission regions, and presents new opportunities to test (e.g. via mock observations) theoretical models of the accretion disc and BELR well before the new era of microlensed quasar discoveries begins. A parameter survey does not remove the need for detailed modelling of individual systems: for example, simultaneous multi-image fits to light curves including dynamical motions of the stellar lens populations, requiring generation of magnification maps for each observation epoch, as per Poindexter & Kochanek (2010a).

This paper is organised as follows. In Section 2, we discuss the theoretical considerations for a survey of the entirety of convergence-shear parameter space on a GPU-based computing cluster. We discuss magnification map size and resolution considerations, and use simulation time estimates based on the results of Thompson et al. (2010) to inform a realistic simulation strategy. In Section 3 we illustrate one possible use for our survey by examining the systematic effects on accretion disc constraints in the lensed quasar Q2237+0305 when the lens macro-model is varied. We present our conclusions in Section 4.

²1 teraflop/s = 10^{12} floating point operations per second.

³The gSTAR facility was part-funded by Astronomy Australia Limited through the Australian Federal Government’s Education Investment Fund.

Throughout this paper, a cosmology with $H_0 = 70\text{kms}^{-1}\text{Mpc}^{-1}$, $\Omega_m = 0.3$ and $\Omega_\Lambda = 0.7$ is assumed.

2. Survey design

In this section, we discuss the theoretical considerations that inform the choices of parameters for a high-resolution, cosmological microlensing parameter space survey. We discuss the ways in which observational constraints shape the magnification map sizes and resolutions that are required to produce a useful resource for the microlensing community.

There are two techniques for constraining quasar structure from microlensing observations: analysis of time-dependent light curves (e.g. Wyithe et al. 2000; Kochanek 2004), or single epoch observations (Witt et al. 1995; Bate et al. 2008). Both rely upon a lens model, which is used to generate magnification maps that describe the fluctuation of magnification induced by the microlenses, projected onto the source plane. The lens model is defined in terms of the (external) shear, γ , and the convergence, κ . Shear describes the distortion applied to images and is assumed to be dominated by matter in the host galaxy, however any matter along the line of sight to the source can contribute. Convergence describes the focussing power of the (macro-)lens, and includes contributions from both smooth matter, κ_s , and compact objects, κ_* , according to $\kappa = \kappa_s + \kappa_*$. We define the smooth matter fraction to be

$$s = \kappa_s / \kappa. \quad (1)$$

Once a set of model parameters have been defined, a magnification map can be generated using the gravitational lens equation in the following form:

$$\mathbf{y} = \begin{pmatrix} 1 - \gamma & 0 \\ 0 & 1 + \gamma \end{pmatrix} \mathbf{x} - \kappa_s \mathbf{x} - \sum_{i=1}^{N_*} m_i \frac{(\mathbf{x} - \mathbf{x}_i)}{|\mathbf{x} - \mathbf{x}_i|^2} \quad (2)$$

which relates the two-dimensional location of a light ray, \mathbf{x} , with a source position, \mathbf{y} , for

$$N_* = \frac{\kappa_* A}{\pi \langle M \rangle} \quad (3)$$

compact lenses distributed in an ellipse of area A , at lens plane coordinates, \mathbf{x}_i , and with mean lens mass, $\langle M \rangle$.

Using Equation (2) to shoot light rays at known positions backwards through the lens plane to the source plane, we can count the number of rays reaching each pixel, N_{ij} . Comparing these values to the average number of light rays per pixel if there were no lensing,

N_{rays} , we obtain estimates for the per pixel magnification:

$$\mu_{ij} = N_{ij}/N_{\text{rays}}. \quad (4)$$

For large N_* and large total number of light rays, the direct computation of Equation (2) on a single-core CPU is not feasible. The hierarchical tree-code (Wambsganss 1990; Wambsganss 1999) overcomes this limitation by replacing the N_* lenses with a reduced number of higher-mass pseudo-lenses. A similar approach is used in the Fourier method (Kochanek 2004), where the lens and source planes are treated in a periodic fashion, which helps reduce the total number of light rays required, and also removes the edge effects, making more of the magnification map usable for analysis. The tessellation approach (Mediavilla et al. 2006; Mediavilla et al. 2011) reduces the total number of light rays by using a sophisticated mapping of polygonal regions from the lens plane to the source plane.

While all of these algorithms lead to improved computational efficiency, they do this at the expense of algorithmic (and hence implementation) simplicity. The high level of parallelism in the direct ray-shooting algorithm, coupled with the arithmetic intensity inherent in Equation (2), are ideal attributes for implementation on a GPU. For details of the GPU-D code, including optimisation issues and timing tests, see Thompson et al. (2010). For timing and accuracy comparisons between GPU, hierarchical tree codes and parallel large data codes, see Bate et al. (2010). Mediavilla et al. (2011) report on a timing comparison between an improved implementation of the tessellation method and the GPU-D results from Bate et al. (2010): they find a two order of magnitude improvement in computational efficiency, but the total run-times of the two approaches were comparable.

As the three (currently) CPU-only approaches for generating magnification maps share a high-degree of parallelism, particularly through the need to calculate deflections of many light rays, opportunities exist for their implementation on massively parallel architectures. Such work is beyond the scope of this present paper. We adopt the viewpoint that we have a working GPU ray-shooting code, and have access to a ~ 100 teraflop/s supercomputing facility, gSTAR, and hence present what could be achieved now. Any progress in reducing the total computation time should be traded off with the additional amount of time required to implement an alternative, more complex, solution (Fluke et al. 2011).

2.1. Map size and resolution

In microlensing simulations, we run into the usual conflict between map size (measured in units of the Einstein radius) and map resolution. We need maps that have sufficient resolution to resolve the very inner regions of quasar accretion discs ($\sim 10^{14}$ cm; see for

example the analysis of RXJ1131-1231 in Dai et al. 2010), and sufficient size to map out quasar broad emission lines ($\sim 10^{17}$ cm for the CIII]/CIV/MgII lines; see for example the microlensing analysis of Wayth et al. 2005, or the reverberation mapping analysis of Kaspi et al. 2007). One option is to provide two sets of maps with sizes and resolutions tuned to the extreme physical scales for the accretion disk and BELR. In light of recent multi-wavelength studies of accretion disk sizes and structures (Poindexter et al. 2008; Morgan et al. 2010; Blackburne et al. 2011; Mosquera et al. 2011a), the approach we adopt is a single map that spans both physical scales. This permits the use of self-consistent quasar models for studying future, simultaneous multi-wavelength observations extending from accretion disk to BELR scales.

To set the pixel resolution required, we take the last stable orbit of a Schwarzschild black hole of mass, M_{bh} :

$$R_{ISCO} = \frac{6GM_{bh}}{c^2} = 8.86 \times 10^{13} \left(\frac{M_{bh}}{10^8 M_{\odot}} \right) \text{ cm}, \quad (5)$$

where G is the gravitational constant and c is the speed of light. We define this value for a $10^8 M_{\odot}$ black hole as the fiducial radius, R_{ISCO}^{fid} . For a fixed map size, the pixels required to reach exactly this resolution will vary from system to system, as the Einstein radius depends on the angular diameter distances, D_{ij} , between the observer, o , lens, d , and source, s . Projected onto the source plane, the Einstein radius is:

$$\eta_0 = \sqrt{\frac{D_{os} D_{ds}}{D_{od}} \frac{4G \langle M \rangle}{c^2}}, \quad (6)$$

for a microlens with mean mass, $\langle M \rangle$. For a background quasar at redshift $z = 2.0$, a lens at $z = 0.5$, and a mean microlens mass $\langle M \rangle = 0.3 M_{\odot}$, the Einstein Radius is 2.87×10^{16} cm.

How, then, do we determine the required number of pixels? We start by considering 59 of the currently known lensing systems with redshifts available for both source and lens using data from the CASTLES Survey (this is a more conservative choice than Mosquera et al. 2011b, who used estimates of lens redshifts to build up a sample consisting of 87 systems). Choosing $\langle M \rangle = 0.3 M_{\odot}$, we calculate the mean Einstein radius $\langle \eta_0 \rangle$ and its standard deviation to be:

$$\langle \eta_0 \rangle = (2.93 \pm 1.20) \times 10^{16} h_{70}^{-1/2} \left(\frac{\langle M \rangle}{0.3 M_{\odot}} \right)^{1/2} \text{ cm}. \quad (7)$$

The Einstein radius of each system, along with the mean and standard deviation, are plotted in Figure 1. To achieve our target pixel resolution, R_{ISCO}^{fid} , our maps would require an average of ~ 330 pixels per η_0 .

The two systems with unusually large Einstein radii are Q2237+0305 and MG1549+3047. In both cases, the large Einstein radii are a result of lensing galaxies at unusually low redshifts: $z_d = 0.04$ for Q2237+0305, and $z_d = 0.11$ for MG1549+3047. The latter is also an extended source seen as a radio ring (Lehar et al. 1993), and is not known to exhibit microlensing, so it is an atypical object. Removing these two systems essentially does not change the measured mean Einstein radius, but reduces the standard deviation by a factor of 1.79. We make no comment here on selection effects that might bias this measurement; we simply note that the known sources are a reasonable place to start. Existing gravitationally lensed quasars have been discovered using a wide variety of techniques (see Kochanek 2006), which are likely to be developed and refined in the era of large synoptic surveys.

Next, we determine the preferred physical size for the magnification maps. There are two main considerations here: that they be large enough to conduct simulations of quasar BELRs, and that they are wide enough to allow long light curves to be simulated.

Assuming the quasar $H\beta$ BELR radius-luminosity relation (Bentz et al. 2009), $R_{BELR} \propto L^{0.519}$, holds for high-luminosity, high-redshift quasars (see Kaspi et al. 2007), we can estimate the expected BELR radius. Mosquera et al. (2011b) performed this calculation for their sample of 87 lensed quasars; for the 44 that overlap with our sample, the estimated mean $H\beta$ BELR and its standard deviation are $(1.71 \pm 1.47) \times 10^{17}$ cm, or $(5.84 \pm 5.01)\langle\eta_0\rangle$.

Under the usual criterion that sources with sizes smaller than or approximately equal to the Einstein radius can be significantly microlensed, this suggests that $H\beta$ BELRs are generally too large to undergo significant microlensing. However, the BELR is known to be stratified, with higher ionisation lines emitted closer to the central source. In NGC 5548, for example, the CIV line is emitted from a region a factor of two smaller than the $H\beta$ line (see for example Peterson et al. 1991; Dietrich et al. 1993). Microlensing estimates of the size of the CIII] emission region in the lensed quasar Q2237+0305 suggest a radius similar to the Einstein radius for that source (Wayth et al. 2005; O’Dowd et al. 2010; Sluse et al. 2011). In line with the microlensing analyses of Abajas et al. (2002) and Lewis & Ibata (2004), we therefore assume an approximate outer radius for the high ionisation BELR of $1\eta_0$.

A map with side length $50\eta_0$, convolved with a $1\eta_0$ radius BELR, would provide ~ 500 statistically independent data points [taking into account edge effects due to convolution – these can be avoided using the Fourier method (Kochanek 2004)]. This drops dramatically if the BELR is much larger than $1\eta_0$, however repeat generation of statistically independent maps allows us to compensate for this drop off. A $50^2\eta_0$ map would require $\sim 16500^2$ pixels in order to resolve R_{ISCO}^{fid} .

Fortunately, it appears that the effective velocities of lensed quasars are likely to be

small enough that a map large enough to enable simulations of quasar BELRs will also be large enough to allow adequate sampling of microlensing lightcurves. Mosquera et al. (2011b) estimated that the average Einstein radius crossing time (the time taken for a source to travel a single Einstein radius) for a sample of 90 gravitationally lensed quasars peaks at ~ 23 years, with a range of 8 to 44 years, assuming a mean microlens mass of $\langle M \rangle = 0.3M_{\odot}$. We can therefore simulate observations of duration ~ 10 years comfortably with a magnification map large enough for BELR simulations.

2.2. Timing

To further refine our choice of parameters, we investigate anticipated run times. Using the empirical relationship, T_{GPU} , in Thompson et al. (2010) for a 4-GPU NVIDIA S1070 Tesla unit:

$$T_{\text{GPU}} = 1.4 \times 10^4 \left(\frac{N_{\text{pix}}}{4096^2} \right) \left(\frac{N_*}{10^6} \right) \left(\frac{N_{\text{rays}}}{100} \right) \text{sec} \quad (8)$$

we can estimate the likely run time for any given magnification map. We have not estimated times for the hierarchical code, but note that we expect them to be longer overall based on Figure 3 of Bate et al. (2010).

Thompson et al. (2010) obtained a sustained processing performance of 1.28 teraflop/s on the S1070, which is approximately half the nominal peak performance (2.488 teraflop/s). We note that quoted peaks are rarely achieved in scientific computations, as they typically require more than a dual-issued multiply and addition per GPU clock cycle. Assuming this half-peak performance can also be obtained with gSTAR₁₀₀ (gSTAR₆₀₀), we can expect approximately 50 (300) teraflop/s performance utilising the entire facility – an optimistic viewpoint that ignores real-world scheduling issues and the needs of other gSTAR users.

Following Bate et al. (2010), we set $N_{\text{rays}} = 1000$, as this was found to be sufficient for the parameters explored in that paper, and N_{pix} is allowed to vary in line with the discussion in Section 2.1. The remaining unknown in Equation (8) is the number of microlenses, N_* , for each (κ, γ) pair, which we calculate from Equation (3).

We also need to determine the total number of (κ, γ) combinations to cover parameter space. To avoid making any assumptions about the particular lens system each parameter combination represents, we suggest that uniform tiling of κ - γ parameter space is the most conceptually appealing approach. It is likely that a single (κ, γ) combination will be relevant for more than one lensing system due to degeneracies in η_0 . By examining published macro-model parameters for known microlensed quasars (see Table 1 and red symbols in Figure 2) we see that choosing a maximum $\kappa = \gamma = 1.7$ gives us good coverage. We choose uniform

increments $\Delta\kappa = \Delta\gamma = 0.01$, consistent with the accuracy of most of the quoted macrolens models. This results in a 170×171 sampling of κ - γ parameter space ($\kappa = 0.0$ is excluded, as in this case there are no microlenses).

We obtain timing results for 10 values of the smooth matter fraction $s = \kappa_s/\kappa$ per (κ, γ) combination. The smooth matter fraction ranges from $0 \leq s < 1$ in increments of $\Delta s = 0.1$. For a given (κ, γ) combination, increasing the smooth matter fraction decreases the number of stars N_* . This is accounted for in our timing results.

We note that although we have attempted to collate all the (κ, γ) combinations in the literature for Table 1, the list may not be complete. In addition, many authors publish enough information on lens macromodels to extract convergences and shears, but do not quote the values explicitly (see for example Table 6 in Blackburne et al. 2011). We do not include such models in our analysis.

Timing contour plots are provided in Figures 2 and 3. The grayscale in both figures ranges from 0 hours (white) to greater than or equal to 24 hours (black). Note that these are actual hours, not device hours.⁴ Overplotted in both figures (red stars) are the models from the literature (see Table 1). Figure 2 shows the complete timing; the white line indicating points where $(1 - \kappa - \gamma)$ or $(1 - \kappa + \gamma)$ equal zero corresponds to magnification maps that are formally infinite in size, and hence are excluded from our computation. Figure 3 shows timing coverage with regions requiring > 1 gSTAR₁₀₀ day to process masked out.

In Table 2, we present six possible strategies for a GPU-enabled microlensing parameter survey. The first, labelled ‘Complete’, assumes that there are no limitations on the time we can run the survey. Parameter space is completely covered, at the map size and resolution that best suits the large microlensing simulations we would ideally like to run (see Section 2.1). Obviously, this parameter set is impractical; it would require running gSTAR₁₀₀ (gSTAR₆₀₀) non-stop for ~ 115 (~ 19) years!

In the ‘Realistic’ strategy, we sacrifice both map size and pixel resolution in order to speed up the time to complete the simulations. In addition, we exclude from this strategy any magnification map that requires more than 1 gSTAR₁₀₀ (gSTAR₆₀₀) day to simulate. This amounts to 739 (215) excluded combinations of κ and γ , or ~ 4 (~ 1) percent of the total number of simulations. The simulation time is a more reasonable ~ 414 gSTAR₁₀₀ days (~ 167 gSTAR₆₀₀ days).

Simulation strategy ‘Stage 1’ gives an indication of the time required to produce one

⁴These are based on our estimate of processing on the entire cluster at 50 (300) teraflop/s, so that 1 gSTAR₁₀₀ (gSTAR₆₀₀) hour corresponds to $\sim 10^{17}$ ($\sim 10^{18}$) computations in one real hour.

magnification map for each of the model parameters in Table 1. All of the models in that table, representing most (if not all) microlensing models in the literature, would be simulated in ~ 122 gSTAR₁₀₀ days (~ 40 gSTAR₆₀₀ days) using GPU-D. Starting with this strategy, successive processing stages can then fill in the rest of parameter space, moving outwards in regions centred around the current known models (Stages 2–4).

We note that a significant amount of simulation time is spent in maps where $(1 - \kappa - \gamma)$ or $(1 - \kappa + \gamma)$ are close to zero. We have chosen not to include maps with simulation times greater than 1 gSTAR day in our timing. If this cutoff were reduced to 1 gSTAR hour, the ‘Realistic’ strategy would take ~ 80 gSTAR₁₀₀ days (~ 34 gSTAR₆₀₀ days), with 1617 (657) fewer (κ, γ) combinations.

2.3. Data products

Considering the total (unmasked) κ – γ parameter space sampled $170 \times 171 = 29070$ times for a single smooth matter value, and with no repeat maps, the total uncompressed data volume is ~ 53 TB. With consideration of appropriate data types, file formats, the use of compression, and an appropriate database infrastructure to handle queries and map retrieval, we assert that data storage and service is reasonable.

Magnification maps do not have negative values, so we can use an unsigned data type. For the parameters we propose, an unsigned short integer (16-bit) should be sufficient in most cases (for typical $N_{\text{rays}} \sim 1000$), as this gives us a range from $0 \dots S_{\text{max}} = 65536$ discrete values. If there are cases where individual pixel values are $N_{ij} > S_{\text{max}}$, it is unlikely that there are S_{max} distinct magnification values. In such a case, pixel values can be remapped into the range $0 \dots S_{\text{max}}$, and an index array can be built and stored as metadata. In uncompressed form, and writing maps in a binary file format, a single $N_{\text{pix}} = 10000^2$ map requires 191 MB of storage.⁵

To examine the likely effects of compression, we generate ten maps with randomly assigned values (up to S_{max}) for each pixel. We then trial two standard Unix compression tools, `gzip` and `bzip2`, and record the compression ratio and the times to compress and decompress. We find that `gzip` compresses the random maps consistently to 171 MB with compression and decompression times below 16 sec and 5 sec respectively.⁶ Compare this with 157 MB

⁵We use computing notation where 1 MB = 1 megabyte = 1024 kilobytes, and similarly for gigabyte (GB), terabyte (TB) and petabyte (PB).

⁶Measured on a 2.8 GHz, Intel Core 2 Duo, MacBook Pro, so these are upper limits.

file sizes for `bzip2`, and < 38 sec for compression and < 17 sec for decompression.

We expect compression of real maps to be somewhat better than random pixels, as the range of per pixel values should be lower than a uniform distribution over $0 \dots S_{\max}$. The presence of caustic structures means that there are sequences of repeated values in the maps, which tends to aid with the run-length encoding of `gzip`, and the block-based compression of `bzip2`. We tested compression of a magnification map with $\kappa = 0.416$, $\gamma = 0.471$, corresponding to the $\beta = 1.0$ model for image *A* in Q2237+0305 in Witt et al. (1995). For a 10000^2 -pixel map, and $N_{\text{rays}} = 1000$, the count range was $15 \leq N_{ij} \leq 7060$. In this case, `gzip` and `bzip2` reduced the file size to 113 MB and 80 MB respectively. Times to compress and uncompress the map were 23 sec and 5 sec for `gzip` and 26 sec and 13 sec for `bzip2`. Despite the slightly longer decompression times, which is actually the more critical factor for accessing data stored on disk in compressed form, our testing suggests that `bzip2` is the preferred alternative, with likely compression ratios between 40 per cent and 78 per cent. These estimates are consistent with the compression ratios of 2.5 (40 per cent) to 3 (33 per cent) for OGLE data reported by Poindexter & Kochanek (2010a).

The overhead in decompressing any given map for analysis is small compared to the time taken to generate the map or to transfer large numbers of maps over Ethernet. As the cost per TB of data storage continues to decrease at a rapid rate, we conclude that data storage and access, even with repeat maps and sampling of smooth matter values, is not a significant concern. An efficient, Web-based data delivery mechanism would be required to serve sets of maps on the basis of user requests, and we are currently considering options.

3. First Application

We now present an example of one possible use for a microlensing parameter survey. In this section we analyse the effect of varying lensing parameters (specifically κ and γ) on accretion disc constraints.

As discussed in Section 1, lens macro-models are not uniquely determined. In systems where a wealth of observational data is available, complex models of the mass distribution in the lensing galaxy can be constructed (see for example the Q2237+0305 model of Trott et al. 2010). More often, relatively simple parametric models are used to describe the lens mass distribution. These models are typically found to fit the lensed image positions adequately within observational errors, although additional mass components (perhaps due to other nearby galaxies, e.g. Pooley et al. 2006) are sometimes required.

The main uncertainty in these models is the percentage of the surface density in smoothly

distributed matter. This uncertainty has been included in many microlensing analyses, either as a free parameter in accretion disc measurements, or as the parameter of interest in analyses of lens dark matter fractions (see especially Mediavilla et al. 2009; Bate et al. 2011; Pooley et al. 2011).

This uncertainty is typically confronted in one of two different ways. In the first technique, the galaxy is modelled with a de Vaucoulers profile embedded in a Navarro-Frenk-White (NFW) halo (e.g. Morgan et al. 2006; Poindexter et al. 2008; Chartas et al. 2009; Morgan et al. 2010; Dai et al. 2010). The mass to light ratio is varied, typically from 1 (no NFW halo) to 0.1 (NFW halo dominates the mass distribution). This results in a sequence of lens macro-models, from which microlensing convergences and shears can be extracted.

In the second technique, a single macro-model is produced (usually a singular isothermal ellipse with external shear) to describe the lensing galaxy (e.g. Bate et al. 2008; Mediavilla et al. 2009; Blackburne et al. 2011). A single set of microlensing convergences and shears are obtained from this model. The unknown smooth matter fraction is then accounted for by allowing the smooth κ_s and stellar κ_* components of the convergence to vary, subject to the constraint $\kappa = \kappa_s + \kappa_*$. We have assumed this second technique in our discussion on survey design, however we note that the magnification maps generated by such a survey are equally useful regardless of lens modelling technique.

Since a variety of lens modelling techniques are used, each providing acceptable fits to lensed image positions, it is reasonable to ask whether source quasar parameters can be uniquely determined from microlensing observations. We present a first attempt at a comparison between accretion disc constraints obtained using different lens models here.

We obtain our accretion disc constraints using a single-epoch imaging technique very similar to that presented in Bate et al. (2008) and Floyd et al. (2009). A similar analysis could (and should) be undertaken for the lightcurve technique (Kochanek 2004), but is beyond the scope of this paper.

As an additional benefit, this analysis offers the first opportunity for a direct comparison between accretion disc parameters obtained using the lightcurve technique and the single-epoch imaging technique. The observational data we use, consisting of pseudo-broadband photometry of the lensed quasar Q2237+0305, was presented and analysed using the lightcurve technique in Eigenbrod et al. (2008).

3.1. Method

The single-epoch microlensing simulation technique we use here was first presented in Bate et al. (2008). The goal is to constrain both the radius of the accretion disc σ_0 (at a particular wavelength λ_0), and the power-law index ζ relating accretion disc radius σ to observed wavelength λ . In other words, we model the quasar accretion disc of Q2237+0305 using the following relationship:

$$\sigma = \sigma_0 \left(\frac{\lambda}{\lambda_0} \right)^\zeta \quad (9)$$

where λ_0 is taken to be the central wavelength of the bluest filter in which observations were taken.

The full simulation technique will not be repeated here; it is described in full detail in Section 3 of Bate et al. (2008). There are three key differences between the analysis presented in that paper, and the analysis presented here. First, our Q2237+0305 magnification maps have a fixed microlens mass of $1M_\odot$. Secondly, we use logarithmic Bayesian priors for source radius σ , rather than the constant priors used in our previous analyses. Logarithmic priors ensure that the ratio of prior probability for two values of source size does not depend on the units chosen. This choice also allows us to compare more directly with previous work by other authors. And thirdly, we set the smooth matter percentage in the lensing galaxy at the image positions to zero. This is reasonable because the lensed images lie in the bulge of the lensing galaxy, where stars are expected to dominate the mass distribution.

The result of this analysis technique is an a posteriori probability distribution for radius of the quasar accretion disc in the bluest filter σ_0 , and power-law index ζ relating accretion disc radius to observed wavelength. For our purposes here, we will compare the extracted 68 per cent confidence limits on those two parameters.

We used lensing models for Q2237+0305 from two sources: Witt et al. (1995) and Kochanek (2004). In Witt et al. (1995), the authors modelled four lensing systems with a simple family of lensing galaxy models, parameterised by the power-law index β of the lensing potential with respect to radius r . Microlensing parameters were quoted for three values of β : 0.5, 1.0 (the commonly used singular isothermal sphere model) and 1.5. These three models allow us to test the effect of varying microlensing parameters on our accretion disc constraints. We also use the microlensing parameters from Kochanek (2004), where the lensing galaxy was modelled as a singular isothermal ellipsoid (SIE) with external shear. This allows us to directly compare results obtained using our single-epoch imaging technique with results obtained using the lightcurve technique in Eigenbrod et al. (2008). The parameters

are found in Table 3.

3.2. Observational data

The observational data were obtained from Eigenbrod et al. (2008), who conducted spectroscopic monitoring of Q2237+0305 using the VLT across a three year time period. The data, originally FORS1 spectra, were deconvolved into a broad emission line component, a continuum emission component, and an iron pseudo-continuum. The continuum emission was fit with a power law of the form $f_\nu \propto \nu^{\alpha_\nu}$. Eigenbrod et al. (2008) then split the continuum into six wavelength bands, each with a width of 250Å in the quasar rest frame, and integrated the continuum power-law in each band. The result is pseudo-broadband photometry in six wavebands, with contamination from broad emission lines and the iron continuum removed. Eigenbrod et al. (2008) contains analysis of 39 of their 43 epochs using the lightcurve fitting technique of Kochanek (2004).

Here, we use two epochs of the Eigenbrod et al. (2008) data, separated by a year, and presented in Table 4. We analyse one image combination: B/A . There is no reason in principle why the other images could not also be analysed. Here we choose B/A both to cut down on simulation time, and to allow direct comparison with the Eigenbrod et al. (2008) results (which also only use the B/A image combination). Probability distributions for σ_0 and ζ are obtained for each epoch separately, and then combined together to obtain our final results.

3.3. Results and Discussion

Results are quoted in units of the Einstein radius η_0 (see Equation 6). For Q2237+0305, this is $9.93 \times 10^{16} h_{70}^{-1/2} (\langle M \rangle / 0.3 M_\odot)^{1/2} \text{cm}$. We present 68 per cent confidence limits on ζ and σ_0 for all three models in Table 5. The Eigenbrod et al. (2008) results for their two cases (with and without a velocity prior) are provided for comparison.

The first thing to note is that within their errors, the constraints on both σ_0 and ζ agree for all models. This suggests that at the current level of accuracy, microlensing-based measurements of accretion disc parameters are likely to be consistent even when different lensing models are used.

However, there are some trends in our results which are worth discussing. If we look first at the three Witt et al. (1995) models, we see that as β is increased from 0.5 to 1.5, so the peak value of ζ increases. It is difficult to disentangle what is causing this, however the

most striking variation in the magnification maps as β increases is an increase in the number of microlenses. The $\beta = 1.5$ magnification maps are much more densely packed with caustic structure than their $\beta = 0.5$ counterparts.

If we compare now the results obtained using the single-epoch imaging technique (the Kochanek 2004 lens model) to results obtained using the lightcurve technique (the Eigenbrod et al. 2008 results), there are a few differences. Firstly, the lightcurve technique produces smaller errors. This isn't surprising; we analysed two epochs of data for the single-epoch imaging technique, whereas Eigenbrod and collaborators analysed 39 epochs of data. Secondly, for the same microlensing parameters the single-epoch technique results in slightly lower (although still consistent) values for ζ than the lightcurve technique. Whether this last effect is generically true would require more systems for comparison.

4. Conclusion

As a crucial step in preparing for this influx of new lensed systems that the synoptic survey era promises to deliver, a large-scale exploration of microlensing convergence-shear parameter space is warranted. In this paper, we have described how a such a parameter space survey could be achieved using a modern GPU-based supercomputing facility, and our experiences with the GPU-D code (Thompson et al. 2010; Bate et al. 2010).

Balancing simulation time and theoretical considerations, we suggest that the following is a suitable parameter set for such a survey:

- $0.01 \leq \kappa \leq 1.70$ with increment $\Delta\kappa = 0.01$
- $0.00 \leq \gamma \leq 1.70$ with increment $\Delta\gamma = 0.01$
- $0.0 \leq s < 1.0$ with increment $\Delta s = 0.1$
- $N_{\text{rays}} = 1000$
- $N_{\text{pix}} = 10000^2$
- Map side length = $25\eta_0$

This results in a 170×171 sampling of κ - γ parameter space for each s -value. The number of rays shot per pixel N_{rays} was found to be sufficient to produce accurate magnification maps using the GPU-D code in Bate et al. (2010). The pixel resolution and map size represent an acceptable compromise between the need to resolve the last stable orbit of a Schwarzschild

supermassive black hole R_{ISCO}^{fid} , and the need for large enough maps to conduct microlensing simulations of quasar broad emission line regions and long light curves.

We collated microlensing models from the literature, and used them to suggest ways in which κ - γ parameter space could be masked to reduce simulation time. In addition, a large portion of simulation time is spent in relatively few maps, where $(1 - \kappa - \gamma)$ or $(1 - \kappa + \gamma)$ are close to zero. Masking out any maps with projected simulation times greater than 1 day using the entire facility enables swifter completion of the survey, at the risk of missing some interesting areas of parameter space. With these restrictions in place, we estimate a total simulation time of ~ 414 days utilising the entirety of a 100 teraflop/s facility (gSTAR₁₀₀), or ~ 167 days on a 600 teraflop/s facility (gSTAR₆₀₀). Realistic scheduling requirements for a high-demand supercomputer will increase the total wall-time required, so a staged strategy starting with parameters for the currently known microlensed quasars, would support early science usage.

Finally, we have provided an example of one possible application for a large microlensing parameter survey. We used four different microlensing parameter sets to take a preliminary look at the systematic effects of varying lens models on accretion disc constraints in the lensed quasar Q2237+0305. Although all of the lens models produce results that are consistent within their errors, we note that there are suggestions that models with denser microlensing environments lead to shallower accretion disc temperature profile predictions.

This research was supported under Australian Research Council’s Discovery Projects funding scheme (project number DP0665574). We are grateful to Alex Thompson for his work on the GPU-D code. Our referee provided very helpful suggestions, that improved the quality of the work.

Facilities: VLT:Kueyen (FORs1).

REFERENCES

- Abajas, C., Mediavilla, E., Muñoz, J. A., Popović, L. Č., & Oscoz, A. 2002, ApJ, 576, 640
- Abajas, C., Mediavilla, E., Muñoz, J. A., Gómez-Álvarez, P., & Gil-Merino, R. 2007, ApJ, 658, 748
- Anguita, T., Schmidt, R. W., Turner, E. L., Wambsganss, J., Webster, R. L., Loomis, K. A., Long, D., McMillan, R. 2008, A&A, 480, 327
- Barsdell, B. R., Barnes, D. G., & Fluke, C. J. 2010, MNRAS, 408, 1936

- Bate, N. F., Webster, R. L., & Wyithe, J. S. B. 2007, MNRAS, 381, 1591
- Bate, N. F., Floyd, D. J. E., Webster, R. L., Wyithe, J. S. B., 2008, MNRAS, 391, 1955
- Bate, N. F., Fluke, C. J., Barsdell, B. R., Garsden, H., & Lewis, G. F. 2010, New A, 15, 726
- Bate, N. F., Floyd, D. J. E., Webster, R. L., & Wyithe, J. S. B. 2011, ApJ, 731, 71
- Bentz, M. C., Peterson, B. M., Netzer, H., Pogge, R. W., & Vestergaard, M. 2009, ApJ, 697, 160
- Blackburne, J. A., Pooley, D., Rappaport, S., & Schechter, P. L. 2011, ApJ, 729, 34
- Chartas, G., Kochanek, C. S., Dai, X., Poindexter, S., & Garmire, G. 2009, ApJ, 693, 174
- Dai, X., Kochanek, C. S., Chartas, G., Kozłowski, S., Morgan, C. W., Garmire, G., Agol, E. 2010, ApJ, 709, 278
- Dietrich, M., Kollatschny, W., Peterson, B. M., et al. 1993, ApJ, 408, 416
- Eigenbrod, A., Courbin, F., Meylan, G., Agol, E., Anguita, T., Schmidt, R.W., Wambsganss, J. 2008, A&A, 490, 933
- Fluke, C. J., Barnes, D. G., Barsdell, B. R., & Hassan, A. H. 2011, PASA, 28, 15
- Floyd, D.J.E, Bate, N.F., Webster, R.L. 2009, MNRAS, 298, 233
- Gómez-Álvarez, P., Mediavilla, E., Muñoz, J. A., Sánchez, S.F., Oscoz, A., Prada, F., & Serra-Ricart, M. 2006, ApJ, 645, 5
- Irwin, M.J., Webster, R.L., Hewett, P.C., Corrigan, R.T., Jędrzejewski, R.I. 1989, AJ, 98, 1989
- Ivezić, Z., et al. 2008, preprint arXiv:0805.2366v1 [astro-ph]
- Kaspi, S., Brandt, W. N., Maoz, D., Netzer, H., Schneider, D. P., & Shemmer, O. 2007, ApJ, 659, 997
- Keeton, C.R., Burles, S., Schechter, P.L., Wambsganss, J. 2006, ApJ, 639, 1
- Keller, S. C., Schmidt, B. P., Bessell, M. S., Conroy, P. G., Francis, P., Granlund, A., Kowald, E., Oates, A. P., Martin-Jones, T., Preston, T., Tisserand, P., Vaccarella, A., Waterson, M. F. 2007, PASA, 24, 1

- Kirk, D.B., Hwu, W.-m. W. 2010, *Programming Massively Parallel Processors* (Burlington: Morgan Kaufman Publishers)
- Kochanek, C.S. 2004, *ApJ*, 605, 58
- Kochanek, C. S. 2006, in *Saas-Fee Advanced Course 33, Gravitational Lensing: Strong, Weak and Micro*, ed. G. Meylan, P. Jetzer, & P. North (Berlin: Springer), 453
- Lehar, J., Langonst, G. I., Silber, A., Lawrence, C. R., & Burke, B.F. 1993, *AJ*, 105, 847
- Lewis, G. F., Irwin, M. J., Hewett, P. C., & Foltz, C. B. 1998, *MNRAS*, 295, 573
- Lewis, G.F., Ibata, R.A. 2004, *MNRAS*, 348, 24
- Mediavilla, E., Muñoz, J. A., Lopez, P., Mediavilla, T., Abajas, C., Gonzalez-Morcillo, C., Gil-Merino, R., 2006, *ApJ*, 653, 942
- Mediavilla, E., Mediavilla, T., Muñoz, J. A., Ariza, O., Lopez, P., Gonzalez-Morcillo, C., & Jimenez-Vicente, J., 2011, *ApJ*, 741, 42
- Mediavilla, E., et al. 2009, *ApJ*, 706, 1451
- Mediavilla, E., et al. 2011, *ApJ*, 730, 16
- Morgan, C. W., Kochanek, C. S., Morgan, N. D., Falco, E. E. 2006, *ApJ*, 647, 874
- Morgan, C. W., Eyler, M. E., Kochanek, C. S., Morgan, N. D., Falco, E. E., Vuissoz, C., Courbin, F., & Meylan, G. 2008, *ApJ*, 676, 80
- Morgan, C. W., Kochanek, C. S., Morgan, N. D., & Falco, E. E. 2010, *ApJ*, 712, 1129
- Mosquera, A. M., Muñoz, J. A., Mediavilla, E., & Kochanek, C. S. 2011, *ApJ*, 728, 145
- Mosquera, A. M., Kochanek, C. S. 2011, *ApJ*, 738, 96
- O’Dowd, M., Bate, N. F., Webster, R. L., Wayth, R., & Labrie, K. 2010, arXiv:1012.3480
- Oguri, M. 2007, *ApJ*, 660, 1
- Oguri, M., & Marshall, P. J. 2010, *MNRAS*, 587
- Peterson, B. M., Balonek, T. J., Barker, E. S., et al. 1991, *ApJ*, 368, 119
- Poindexter, S., Kochanek, C. S. 2010a, *ApJ*, 712, 658
- Poindexter, S., Kochanek, C. S. 2010b, *ApJ*, 712, 668

- Poindexter, S., Morgan, N., & Kochanek, C. S. 2008, *ApJ*, 673, 34
- Pooley, D., Blackburne, J. A., Rappaport, S., Schechter, P. L., & Fong, W.-f. 2006, *ApJ*, 648, 67
- Pooley, D., Rappaport, S., Blackburne, J., Schechter, P. L., Schwab, J., & Wambsganss, J. 2009, *ApJ*, 697, 1892
- Pooley, D., Rappaport, S., Blackburne, J. A., Schechter, P. L., & Wambsganss, J. 2011, arXiv:1108.2725 [astro-ph.HE]
- Rix, H.-W., Schneider, D. P., & Bahcall, J. N. 1992, *AJ*, 104, 959
- Richards, G.T., et al. 2004, *ApJ*, 610, 679
- Schmidt, R., Webster, R. L., & Lewis, G. F. 1998, *MNRAS*, 295, 488
- Schmidt, R. W., & Wambsganss, J. 2010, *General Relativity and Gravitation*, 62
- Schneider, D. P., Turner, E. L., Gunn, J. E., Hewitt, J. N., Schmidt, M., & Lawrence, C. R. 1988, *AJ*, 95, 1619
- Sluse, D., et al. 2011, *A&A*, 528, A100
- Thompson, A.C., Fluke, C.J., Barnes, D.G., Barsdell, B.R. 2010, *New Astronomy*, 15, 16
- Trott, C. M., Treu, T., Koopmans, L. V. E., & Webster, R. L. 2010, *MNRAS*, 401, 1540
- Wambsganss, J. 1990, Ph.D. Thesis, Munich Univ.
- Wambsganss, J. 1999, *Journal of Computational and Applied Mathematics*, 109, 353
- Wambsganss, J. 2006, in *Gravitational Lensing: strong, weak and micro.Saas-Fee Advanced Course 33*, ed. G.Meylan, P.Jetzer, & P. North (Berlin: Springer), 453
- Wambsganss, J., & Paczynski, B. 1994, *AJ*, 108, 1156
- Wayth, R. B., O’Dowd, M., & Webster, R. L. 2005, *MNRAS*, 359, 561
- Witt, H. J., Mao, S., Schechter, P. L. 1995, *ApJ*, 443, 18
- Wyithe, J. S. B., Webster, R. L., & Turne, E. L. 2000, *MNRAS*, 318, 762
- Wyithe, J. S. B., Agol, E., & Fluke, C. J. 2002, *MNRAS*, 331, 1041

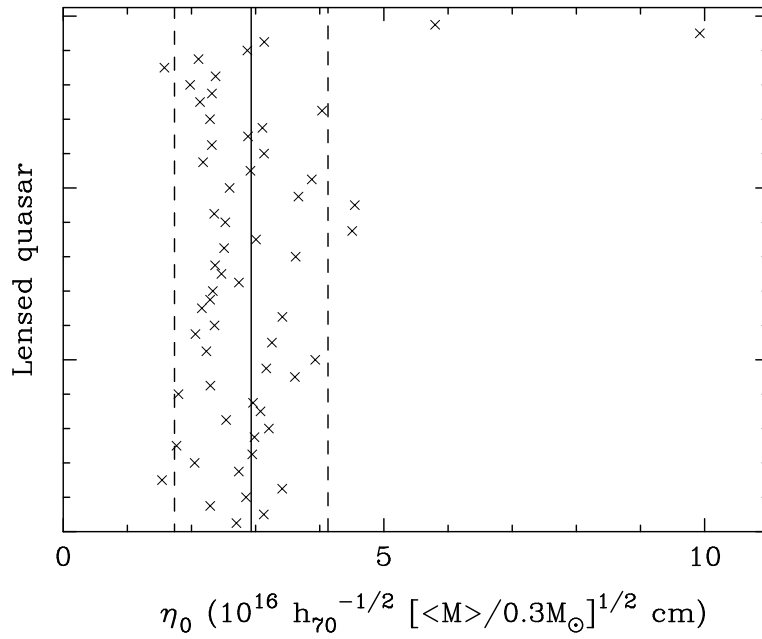


Fig. 1.— The Einstein radius projected on to the source plane η_0 for each of the 59 lensing systems with both source and lens redshifts on the CASTLES Survey webpage (<http://cfa-www.harvard.edu/glensdata/>). The Einstein radius is calculated for a $0.3M_{\odot}$ lens. The solid line indicates the mean η_0 , and the dashed lines the standard deviation.

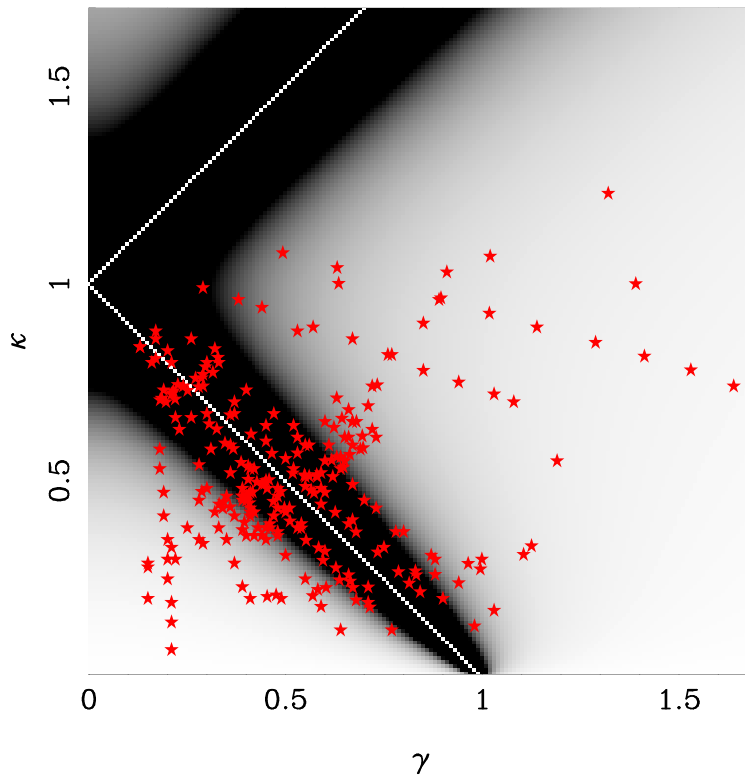


Fig. 2.— A contour plot showing simulation time for a magnification map with a given combination of κ and γ . The colour gradient ranges from 0 hours (black) to 24 hours (white). Overlaid are the existing models taken from the literature (Table 1). Times were calculated using Equation 8, assuming maps with a side-length of $25\eta_0$, $N_{\text{pix}} = 10,000^2$ and $N_{\text{rays}} = 1000$.

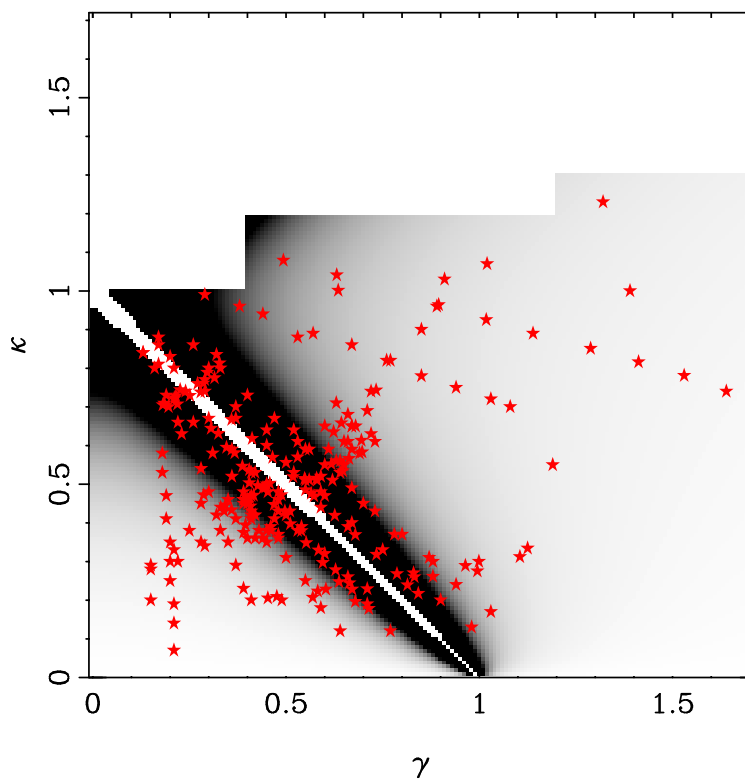


Fig. 3.— A contour plot showing simulation time for a magnification map with a given combination of κ and γ , with maps that require simulation time greater than 1 gSTAR₁₀₀ day masked out. The colour gradient ranges from 0 hours (black) to 24 hours (white). Overlaid are the existing models taken from the literature (Table 1). Times were calculated using Equation 8, assuming maps with a side-length of $25\eta_0$, $N_{\text{pix}} = 10,000^2$ and $N_{\text{rays}} = 1000$.

Table 1. Known microlens models and references.

System	N_{models}	Ref.
HE 0047-1756	1	(4)
QJ 0158-4325	10	(7)
MG 0414+0534	3	(13)
HE 0435-1223	1	(4)
HE 0512-3329	1	(4)
SDSS 0806+2006	1	(4)
SDSS 0909+532	2	(4), (5)
SDSS J0924+0219	13	(2), (4), (6)
FBQ 0951+2635	1	(4)
QSO 0957+561	1	(4)
SDSS J1001+5027	1	(4)
SDSS J1004+4112	1	(4)
QSO 1017-207	1	(4)
HE 1104-1805	11	(4), (7)
PG 1115+080	5	(4), (8), (13)
RX J1131-1231	11	(1), (4)
SDSS J1206+4332	1	(4)
SDSS J1353+1138	1	(4)
H1413+117	4	(4), (13)
B J1422+231	1	(4)
SBS 1520+530	1	(4)
WFI J2033-4723	1	(4)
Q2237+0305	12	(3), (9), (10), (11), (12), (13)

References. — (1) Dai et al. 2010; (2) Keeton et al. 2006; (3) Kochanek 2004; (4) Mediavilla et al. 2009; (5) Mediavilla et al. 2011; (6) Morgan et al. 2006; (7) Morgan et al. 2008; (8) Pooley et al. 2009; (9) Rix et al. 1992; (10) Schmidt et al. 1998; (11) Schneider et al. 1988; (12)

Wambsganss & Paczynski 1994; (13) Witt et al. 1995.

Table 2. Simulation strategies.

Strategy	Side length (η_0)	Side length (pixels)	Time (gSTAR ₁₀₀)	Time (gSTAR ₆₀₀)	Notes
Complete	50	16500	115 years	19 years	full parameter space simulation
Realistic	25	10000	414 days	167 days	
Stage 1	25	10000	122 days	40 days	one map at each Table 1 model position
Stage 2	25	10000	177 days	59 days	maps at Table 1 model positions ± 0.01
Stage 3	25	10000	332 days	140 days	maps at Table 1 model positions ± 0.05
Stage 4	25	10000	392 days	157 days	maps at Table 1 model positions ± 0.1

Note. — Parameter space is tiled with a resolution of 0.01 in both κ and γ , and 0.1 in s . All times are estimated, and assume 100% utilisation of gSTAR. The ‘Complete’ strategy assumes no time constraints whatsoever, and is obviously impractical. All subsequent strategies exclude any parameter combinations that require greater than 1 device day per map to simulate, and mask out regions of parameter space containing no models (see Figure 3). Stages 1-4 represent progressive filling of parameter space towards the Realistic strategy. The listed simulation times are cumulative – for example, Stage 2 takes 177 gSTAR₁₀₀ days to complete, but at the end of that time period Stage 1 will also have been simulated.

Table 3. Microlensing parameters for Q2237+0305.

Model	Image	κ	γ	Magnification μ	Ref.
$\beta = 0.5$	<i>A</i>	0.228	0.603	4.3	(1)
	<i>B</i>	0.223	0.582	3.8	
	<i>C</i>	0.289	0.964	-2.4	
	<i>D</i>	0.261	0.880	-4.4	
$\beta = 1.0$	<i>A</i>	0.471	0.416	9.4	(1)
	<i>B</i>	0.464	0.406	8.1	
	<i>C</i>	0.552	0.617	-5.6	
	<i>D</i>	0.515	0.579	-10.0	
$\beta = 1.5$	<i>A</i>	0.728	0.215	36.5	(1)
	<i>B</i>	0.723	0.212	31.3	
	<i>C</i>	0.789	0.296	-23.3	
	<i>D</i>	0.761	0.286	-40.7	
SIE+ γ	<i>A</i>	0.394	0.395	4.7	(2)
	<i>B</i>	0.375	0.390	4.2	
	<i>C</i>	0.743	0.733	-2.1	
	<i>D</i>	0.635	0.623	-3.9	

References. — (1) Witt et al. 1995; (2) Kochanek 2004.

Table 4. Two epochs of observational B/A and C/A flux ratios for Q2237+0305.

Band	Emitted λ_c (Å)	Observed λ_c	B/A	C/A	Date
1	1625 ± 125	4379 ± 337	0.52 ± 0.02	0.31 ± 0.03	2005 November 11
2	1875 ± 125	5053 ± 337	0.51 ± 0.02	0.33 ± 0.03	2005 November 11
3	2125 ± 125	5727 ± 337	0.50 ± 0.01	0.34 ± 0.03	2005 November 11
4	2375 ± 125	6401 ± 337	0.49 ± 0.01	0.35 ± 0.03	2005 November 11
5	2625 ± 125	7074 ± 337	0.48 ± 0.01	0.37 ± 0.03	2005 November 11
6	2875 ± 125	7748 ± 337	0.47 ± 0.01	0.37 ± 0.02	2005 November 11
1	1625 ± 125	4379 ± 337	0.33 ± 0.02	0.28 ± 0.02	2006 November 10
2	1875 ± 125	5053 ± 337	0.34 ± 0.02	0.30 ± 0.02	2006 November 10
3	2125 ± 125	5725 ± 337	0.35 ± 0.01	0.31 ± 0.02	2006 November 10
4	2375 ± 125	6401 ± 337	0.36 ± 0.02	0.33 ± 0.02	2006 November 10
5	2625 ± 125	7074 ± 337	0.37 ± 0.02	0.34 ± 0.02	2006 November 10
6	2875 ± 125	7748 ± 337	0.37 ± 0.01	0.35 ± 0.02	2006 November 10

Note. — Data obtained from Eigenbrod et al. (2008). Photometry was extracted from spectra obtained with the FORS1 spectrograph on the Very Large Telescope (VLT) at the European Southern Observatory (ESO). Filter wavelengths are in the rest frame of the source quasar, located at a redshift of $z_s = 1.695$. Following the Eigenbrod et al. (2008) numbering, the 2005 November 11 dataset is epoch number 17, and the 2006 November 10 dataset is epoch number 28.

Table 5. Accretion disc constraints for three Q2237+0305 models.

Model	Radius σ_0	Power-law index ζ
$\beta = 0.5$	$< 0.15\eta_0$	$0.79^{+0.63}_{-0.37}$
$\beta = 1.0$	$< 0.15\eta_0$	$0.88^{+0.56}_{-0.37}$
$\beta = 1.5$	$< 0.16\eta_0$	$1.40^{+0.83}_{-0.58}$
Kochanek (2004) model	$< 0.21\eta_0$	$0.77^{+0.57}_{-0.34}$
Eigenbrod et al. (2008) velocity prior	$0.16^{+0.12}_{-0.10}\eta_0$	1.2 ± 0.3
Eigenbrod et al. (2008) no velocity prior	$0.69^{+1.30}_{-0.60}\eta_0$	1.1 ± 0.3

Note. — Constraints on radius of the accretion disc in Q2237+0305 at $\lambda_{obs} = 4379\text{\AA}$, and power-law index relating accretion disc radius and observed wavelength of emission. Constraints were obtained using the B/A image combination. Results from Eigenbrod et al. (2008), which were obtained using the lightcurve technique of Kochanek (2004), are provided for comparison.